Characterization of the Spatial Distribution and Evolution of Cerium and Calcium in Laser Produced Plasma

THESIS

Michael G. Rynders, 1st Lt, USAF

AFIT-ENP-MS-21-M-132

DEPARTMENT OF THE AIR FORCE
AIR UNIVERSITY

AIR FORCE INSTITUTE OF TECHNOLOGY

Wright-Patterson Air Force Base, Ohio

AFIT-ENP-MS-21-M-132

CHARACTERIZATION OF THE SPATIAL DISTRIBUTION AND EVOLUTION OF CERIUM AND CALCIUM IN LASER PRODUCED PLASMA

THESIS

Presented to the Faculty

Department of Engineering Physics

Graduate School of Engineering and Management

Air Force Institute of Technology

Air University

Air Education and Training Command

in Partial Fulfillment of the Requirements for the

Degree of Master of Science in Applied Physics

Michael G. Rynders, B.S.

1st Lt, USAF

March 2021

AFIT-ENP-MS-21-M-132

CHARACTERIZATION OF THE SPATIAL DISTRIBUTION AND EVOLUTION OF CERIUM AND CALCIUM IN LASER PRODUCED PLASMA

THESIS

Michael G. Rynders, B.S.
1st Lt, USAF

Committee Membership:

Dr. Anil Patnaik
Chair

Dr. Michael Shattan
Member

Dr. Mark Gragston
Member

AFIT-ENP-MS-21-M-132

Abstract

Understanding plasma plumes and the distribution of plasma species microseconds after their formation has a variety of applications in fields such as hypersonics, explosion and combustion dynamics, and nuclear fireball chemistry. In this work, 532 nm laser light in a pulse doublet configuration was used to produce cerium plasmas in atmospheres of air, vacuum, and argon for spatial analysis. The species spatial distributions were found to show fractionation of the species. This establishes that Ce-II, Ca-I, and Ca-II tend to collocate in a plasma plume with Ce-I being located separately until recombination. CeO_2 powder was pressed with CaO at a ratio of 90-10 to produce calcium doped pellets for use as sputtering targets. Cerium was used in this experiment to serve as a plutonium material surrogate due to its similar chemical and physical properties. Inclusion of calcium impurities allowed the identification of how calcium species locate relative to cerium species in the plume. Tests were primarily conducted at 10 torr and over a time period 0 ns to 5000 ns after the second laser pulse. 1D spatial information was captured along the vertical center of the plasma plume over an 8.43mm field of view. Temperature was estimated using the Boltzmann and Saha-Boltzmann plots and was found to be on the order of $3500 \pm 500K$. Electron density was calculating using the Stark broadening of the Hα line and found to be on the order of $3 \times 10^{16} \pm 1 \times 10^{16}$ cm^{-3}. This leads to the conclusion that the laser-induced plasma is optically thick for a majority of the species and Ce-I and Hα were located on the outer shell of the plasma.

AFIT-ENP-MS-21-M-132

To those who believed in me.

Table of Contents

Page

List of Figures

Figure		Page

Figure Page

Figure Page

List of Tables

List of Acronyms

CaO	Calcium oxide
CeO	Cerium oxide
DC	Direct Current
FWHM	Full Width at Half Maximum
ICCD	Intensified Charge-Couple Device
LED	Light Emitting Diode
LIP	Laser Induced Plasma
LPP	Laser Produced Plasma

CHARACTERIZATION OF THE SPATIAL DISTRIBUTION AND EVOLUTION OF CERIUM AND CALCIUM IN LASER PRODUCED PLASMA

I. Introduction

The mushroom shaped fireball following a nuclear detonation is an iconic representation of the power of the modern age and the looming threat it presents. The threat of a nuclear attack has expanded from primarily a major exchange between world powers to now include the comparatively small, crude devices deployed by non-state actors or by proxy states [1]. Due to the nature of the actor, the identification of the origin of such a devise this will not be straight forward. A potential device could be a one-off locally sourced fabrication, a stolen device, or a deniable acquisition from a declared nuclear state. In relevant scenarios, identifying the origin of the device and details of its design are pivotal challenges to overcome.

The examination of a device's debris and residue is the principle post-detonation strategy for extracting information about the device, its manufacture, and its origin. [2]. From a nuclear forensics perspective the most compelling material is the unburnt nuclear fuel residue. The ratio of isotopic enrichment and other impurities within the residue can give clues to its origin. Depending on the sophistication of the design, a device's mass will normally be on the order of 100 kg, with a fuel mass on the order of 6 kg [3]. However, the mass of material entrained into the fireball from sediment, soil, and other material around ground zero is many orders of magnitude higher [4]. Contingent on the height of the burst, the majority of this mass will be from soil and sediment which is transformed by, intermixes with, and eventually condenses with the material from the bomb case in the fireball. The complexity of the local environment

can range from a relatively simple homogeneous desert soil to an urban setting with its own litany of common to regionally diverse materials.

The macroscopic fallout particles in the immediate vicinity of ground zero will primarily be in the form of glassy chunks created from the frozen droplets of molten sediment [5]. The contributory materials of these molten glassy chunks undergo fractionation; the alteration of the compositional makeup of a piece of fallout after detonation due to the physical, chemical, and radiochemical processes. Fractionation is a complex process that differs based on the physical and chemical properties of the materials involved, the characteristics of the device, and the distance from the point of detonation.

Debris analysis takes some of these chunks of material and utilizes information about the final form and state of the elements post detonation to deconvolve which elements came from the environment versus from the weapon. The importance of understanding debris formation and fractionation extends to areas including but not limited to: nuclear forensics on historical material, improvements to current designs, debris analysis for arms control, radioecological studies, and other related areas.

Experimental nuclear testing is not practical both due to international treaties preventing the testing of nuclear weapons and because measuring the chemical changes during a nuclear fireball can be challenging from an instrumentation perspective [6]. This makes modeling a much more attractive option however these models require experimental data to inform development. While nuclear testing is no longer an option, there is a selection of material and data from historical tests that can provide the needed information.

Work done examining Trinitite, a glassy mineral produced by the U.S. nuclear tests at White Sands Proving Ground, found that plutonium had a strong correlation with calcium rich regions in the debris [7]. The calcium comes from the ubiquitous

mineral calcite, $CaCO_3$, present in most soils which is transformed into CaMgFe rich glass by the fireball, which then intermixes with and eventually entrains material from the fireball [5]. It was found that the calcium rich glass preferentially includes a high concentration of plutonium and uranium [8]. Calcium and plutonium have a known chemical relationship in which calcium is often used to reduce plutonium to its metallic form during processing and environmental remediation [9]. In this case the calcium is acting as a strong reducing agent.

The implications of this collocation tendency extend beyond the purely scientific and are potentially a practical boon. Currently, the location and identification of the forensically interesting fissionogenic material in-situ is challenging due to instrumentation limitations, mass shielding effects, and the trace amounts of material involved [6]. Instead, if a recognizable abundant and stable element can be used as a an easily identifiable *in-situ* tracer, it would make collection of forensically interesting material faster and safer.

Further work has looked specifically at material sucked up into the rising fireball cloud to explore the composition of debris formed inside them as opposed to ground puddle formation [10]. These findings suggest that the spatial relationship is due to the plutonium being associated with the physical properties of the mafic glass and calcium contributes only marginally in leeching additional plutonium into the glass. This conclusion was supported by findings that showed when there is an inclusion of only calcium with no associated glass, there is no associated increase in plutonium concentrations. The resulting conclusion is that the melting temperature and viscosity of the material is the dominant characteristic for determining plutonium concentration incorporation. Crucially, it is unknown if calcium from non-glass sources displays a positive correlation with plutonium.

This work seeks to probe the relationship between calcium and plutonium when

both are sourced directly from a common matrix rather than being intermixed separately. For practical reasons this was done in analogous environment using plasmas generated through more conventional means and using elements more commonly available. While plutonium would be the most representative element to be studied because of its use as a nuclear fuel, it is impractical given the difficulty obtaining the material and the associated safety and experimental challenges. Therefore, it is standard practice to use cerium as plutonium surrogate because it has similar chemical properties and behavior to plutonium [11]. This work used cerium oxide pellets with calcium additives to simulate the relevant chemical makeup of a nuclear fireball.

Instead of using nuclear reactions to generate a plasma, this work used laser pulses to create a Laser Induced Plasma (LIP) to simulate a nuclear fireball plume for spectrscopic analysis. LPP are created with a laser pulse focused on a submillimeter spot to rapidly deposit sufficient energy to ablate a few nanograms of the surface. The energy deposition causes ionization through multiphoton processes and the electrons are further accelerated through the inverse-Bremsstrahlung process by absorbing a photon during a collision. In turn, this causes additional electrons to be liberated by collisions with the energized free electrons and produces an ionization cascade, a process called avalanche ionization resulting in a LIP [12]. Over a period of microseconds, the plasma undergoes ionization, recombination, and eventually cools and dissipates. By examining the atomic emission characteristics of the plasma during this period, a whole range of information about the chemical evolution of the species involved can be investigated.

A further refinement of the this technique uses an initial laser pulse to ablate the material and create an initial plasma plume, and following a delay of a few microseconds, a second pulse is introduced to deposit additional energy which results in orders of magnitude improvements in the signal quality [13]. A 1D spatial slice may

be imaged by focusing the light through a spectrometer slit onto an Intensified Charge-Couple Device (ICCD) with multiple rows. This enables the plasma's properties to be determined at each of these points to build up a cross-sectional view of how the properties change in space. Concatenating a series of spectral images taken at increasingly delayed times, with respect to the second pulse, allows the investigation of the evolution of plasma in time.

Using the aforementioned approximations and techniques, this work seeks to establish a timeline of when and where calcium and cerium species are within a laser-induced plasma and their relative positions as the plasma evolves. This will inform plasma modeling, further the understanding of nuclear fireball chemistry, and have further applications in a wide variety of fields. For instance, the spatial location of species in a plasma has applications in the field of hypersonics, such as tracking material ablated from the surface of a vehicle and how it interacts downstream. Further, it also has applications in combustion chemistry understanding how and where fuel and reactants are and how they move in time. Similarly, tracking the individual species used in plasma deposition manufacturing and how they move in relation to each other could have applications or implications for the final products.

Chapter II of this work outlines some of the theory and fundamentals involved in spectroscopy and the analysis of spectra. A focus is placed on the techniques for estimating and calculating two plasma parameters; temperature and electron density. Discussion is also presented on the underlying assumptions and under what circumstances local thermodynamic equilibrium and optically thin conditions can be invoked.

Chapter III of this work details the experimental methodology that was used to collect the data.

Chapter IV of this work presents the results and details the analysis done. Empha-

sis is on the spatial location of the plasma species, the temperature, and the electron density and how these parameters compare at the spatial locations.

Chapter V of this work concludes the study with discussion of the findings and their significance before offering suggestions for avenues of future work.

Appendix A of this work presents related work using schlieren imaging to capture images of the plume.

II. Theory

To understand the mechanisms and evolution of a plasma there are several fundamental concepts that are useful to review.

Plasma can be described by several attributes with the two most relevant parameters for this thesis being temperature and electron density. Evaluating and determining these parameters allows the plasma to be compared with other plasmas that have equivalent physical conditions generated through nuclear or conventional means. These parameters can be experimentally evaluated through several different techniques; the theory behind them is laid out below.

2.1 Local Thermodynamic Equilibrium

Thermodynamic equilibrium is a critical concept in thermodynamics and serves as a foundation for the majority of the theory pertaining to plasma dynamics [14]. It is therefore important to discuss when and how approximations can be made in the context of thermodynamic equilibrium.

Complete thermodynamic equilibrium is the state of all processes being in balance and for any given volume in the system there is no net energy flow. This means the amount of energy radiated is equal to the amount of energy absorbed by the system and the atomic excitation rate is equal to the deexcitation rate [14]. For experimental dynamically evolving plasmas this is difficult to achieve.

A LPP has a hot central core surrounded by regions of lower temperature. In a 1D view there is a higher temperature along the center expansion with colder regions beneath and on the outside edges. This naturally leads to thermal diffusion between the hotter and colder regions. This energy flow obviously violates the requirement for no transfer of energy out of the system, breaking thermodynamic equilibrium.

Despite complete thermodynamic equilibrium being unachievable for this work there are approximations that can be made allowing for the analysis of plasma parameters using the first-principle derivations. Local thermodynamic equilibrium posits that the parameters do vary but the variation is small enough that from point to point within the plasma can be approximated as being in thermodynamic equilibrium around that region. This approximation is sufficient for the plasma parameter equations to be valid locally.

Like thermodynamic equilibrium, inside local thermodynamic equilibrium there are nuances and different levels of equilibrium. Complete local thermodynamic equilibrium is said to exist when the excitation states are in equilibrium; collisional interactions are dominant, but radiative equilibrium is not satisfied. Even with the relaxation of this condition, it is still too restrictive to be satisfied by a majority of experimental plasmas because resonance transitions tend to have high Einstein spontaneous emission coefficients and so are prone to rapid depopulation which violates the required equilibrium of excitation and deexcitation. Excluding those energy levels below a certain principal quantum number allows the assumption that the plasma is in partial local thermodynamic equilibrium (pLTE). By virtue of the large spontaneous emission coefficient and collisions being the dominant energy transfer mechanism a partial equilibrium is rapidly reached, which a majority of laboratory plasmas are able to achieve [14]. This work focused on pLTE which will be demonstrated and used to support the use of the Boltzmann and Saha-Boltzmann equations [15].

With the above theory laying out the assumptions needed to build a foundation for a theoretical plasma satisfying pLTE conditions, attention now turns to the theory of demonstrating that a given plasma is in pLTE.

The first consideration is that distribution of electron energy follows the Maxwell-Boltzmann distribution. This requires that the mean distance between electrons be

much greater than the de Broglie wavelength [16]. If the inter-electronic distance is closer, the overlap of the wave functions of the particles requires the consideration of quantum mechanical effects and the use of a Fermi-Dirac distribution. This requirement can be expressed in terms of a density by taking the inverse cube of the de Broglie wavelength as shown in Equation 1:

$$N_{\mathrm{e}} \ll \left(\frac{2\pi k m T_{\mathrm{e}}}{h^2}\right)^{3/2} \quad [cm^{-3}], \tag{1}$$

where k is the Boltzmann constant, m is the mass of an electron, T_{e} is the electron temperature, and h is the Planck constant.

As previously mentioned, pLTE conditions require that the collisional rate be greater than the radiative rate to demonstrate that the relaxation time is less than the expansion time. The requirement put forward by the McWhirter criterion is that it should be more than an order of magnitude greater [17]. This criteria can be expressed in terms of electron density in the form shown below in Equation 2:

$$N_{\mathrm{e}} \geq 1.6 \times 10^{12} T^{1/2} \Delta E^3 \quad [cm^{-3}], \tag{2}$$

where N_{e} is the electron density, T is the temperature in K, and ΔE is the energy gap in electron volts.

However, demonstrating that the plasma is within the density bounds and meets these criteria are necessary but not sufficient to establish pLTE conditions [18].

There are several additional techniques used to further validate the pLTE approximation. The technique used in this work looks for agreement in temperatures by comparing the temperatures calculated from the Boltzmann and Saha-Boltzmann plots [15]. An agreement in temperature supports the conclusion that a single temperature is likely adequate for describing the local states/interactions, which is the

pLTE condition.

In Chapter 4, the pLTE condition will be evaluated using the above methods.

2.2 Plasma Optical Thickness

In an ideal system, the photon emitted from the deexcitation of an excited state would travel directly to and be collected by the spectrometer without interference. However, the path between an emitting atom and the spectrometer is not empty even when using a partial vacuum. The attenuation of photons caused by scattering and absorption processes reduces signal-to-noise ratio for a target spectral line. However, these effects tend not to alter the peak shape or relative intensities of the spectral lines. This means the resulting plasma parameter calculations, such as relative concentration, etc, are unaffected.

Self-absorption proves to be more pernicious; it is when a photon emitted from a species is in turn absorbed by another atom of the same species that are prevalent in high-density regions. The absorption and re-emission of these photons distorts and saturates the peaks making them asymmetrical and impairing the validity of analysis based on the peak intensities and widths. In addition, because the atom absorbs a photon of the correct energy it tends to absorb the photons that would form the center of an emission peak. When the peak of an emission line is carved out forming a double peak this is called self-reversal [19].

By virtue of the number of particles involved, self-absorption is presented in a majority of plasmas. The question is the degree to which it affects the emission lines. When the photons from a deexcitation are able to escape the plasma largely without interaction and the lines are intact the plasma is deemed to be optically thin. In contrast, if there is significant distortion of the lines the plasma is dubbed optical thick [19, 15]. Given that atoms of the same species cause self-absorption, a plasma

can be optically thin for one species and optically thick for another.

When designing an experiment, there are several techniques for decreasing and controlling self-absorption. Self-absorption is aggravated by high pressures and concentrations because there are more atoms of the species that can absorb the photons between the emitter and the spectrometer. Decreasing the overhead pressure the plasma is generated under will decrease self-absorption by causing the plasma to expand more. Using a short gate-delay could help observing the emission from the plasma that has a large population of excited species at the early times. In addition, using higher laser energies leads to higher excitation which tends to overcome self-absorption; however, the Stark shift effects could dominate at high-intensities [20].

These considerations influenced the experimental setup and parameters that were used as detailed in Chapter 3, experimental methodology.

2.3 Temperature

Temperature is a key characteristic of the plasma and a very important parameter for plume model validation because it drives which chemical species have sufficient energy to be ionized and what proportion of the atoms will be in each state [21].

One commonly used method for calculating the plasma temperature from spectral data is to compare the relative intensities of two or more widely spaced spectral lines and fitting it to a Boltzmann plot [15]. A basic derivation of the theory is presented below.

Assuming that the system is in pLTE, the Boltzmann distribution for two energy levels, E_i and E_j, is given by:

$$\frac{N_{\mathrm{j}}}{N} = \frac{g_j}{g_i} exp[-\frac{E_j - E_i}{K_B T}], \tag{3}$$

where N_i and N_j are the population densities of the states, g_i and g_j are the statistical weights of the states, k_{B} is the Boltzmann constant, and T is the temperature in Kelvin.

When an excited energy level spontaneously relaxes to a lower level the emission coefficient is given by:

$$\epsilon = \frac{hc}{4\pi\lambda} A N_j, \tag{4}$$

where h is Plancks' constant, c is the speed of light, λ is the wavelength of the emitted light, and A is the transition probability, also called the Einstein spontaneous emission coefficient. The emission coefficient is the intensity of the light emitted and can be replaced with I, the intensity of the line as measured by the spectrometer. Combining Equation 4 and Equation 3 and performing some manipulations results in:

$$ln(\frac{I\lambda}{gA}) = -\frac{1}{k_{\mathrm{B}}T} E + ln(\frac{4\pi Z}{hcN_0}), \tag{5}$$

where E is the energy of the excited state, N_0 is the base species total number density, and Z is the partition function which is temperature dependent through the Boltzmann factor terms.

For our measurement, the intensity of two or more Ce-I lines can be measured and the resulting LHS plotted against the energy level of the lines. If the plasma is in pLTE then a linear fit can be applied and the resulting slope will be:

$$b = \frac{-1}{K_{\mathrm{B}}T}. \tag{6}$$

The second part of the right hand side of Equation 5 contains only constants and so will not affect the slope or temperature and need not be calculated. Typically, the values for g, A, E, and λ for the Ce-I lines were obtained from the NIST database

[22, 23, 24, 25, 26]. Once the slope is obtained the temperature can be extracted through algebraic manipulation.

Another related method for calculating temperature is the Saha-Boltzmann method [15]. Working on a similar theory as the Boltzmann method, the Saha-Boltzmann method compares the relative intensities of two lines but instead of atomic lines it compares the lines from different ionization states. The result is the ionization temperature, but assuming pLTE conditions, there is only a single temperature and the ionization temperature will be equal to the electron temperature.

Following a similar procedure as above the Saha-Boltzmann equation [27] can be arrived as:

$$N_{\mathrm{e}} = \frac{{I_{\mathrm{z}}}^{*}}{{I_{\mathrm{z+1}}}^{*}} 6.04x10^{21}(T)^{3/2} exp(\frac{E_{\mathrm{j,z}} - E_{\mathrm{j,z+1}} - \chi_{\mathrm{z}}}{kT}), \tag{7}$$

with I^{*} is defined as:

$${I_{\mathrm{z}}}^{*} = \frac{I_{\mathrm{z}}\lambda_{\mathrm{ji,z}}}{g_{\mathrm{j,z}}A_{\mathrm{ji,z}}}, \tag{8}$$

where i and j are the lower and upper levels, N_{e} is the electron density, z is the ionization stage, I is the intensity, T is the temperature, E is the transition energy, χ is the ionization energy, λ is the wavelength of the transition, g is the statistical weight of the transition, and A is the transition probability.

Critically, the Saha-Boltzmann equation requires the electron density of the plasma. Fortunately, there exist methods of computing the electron density from the spectral data as discussed in the next section.

2.4 Electron Density

The second key plasma parameter is the plasma's electron density, which is defined as the number density of free electrons present in a plasma. This is an important parameter because the electrons are stripped from the atoms in the plasma producing ions. Hence, the electron density is a good precursor for determined the content and physical state of the target. By knowing both the plasma temperature and electron density the plasma can be classified using a density/temperature plane and thereby related to other plasma created through different mechanisms. Knowing the electron density is also important because, as seen above, it is required for quantifying aspects of the plasma for temperature calculations needed to validate pLTE conditions.

There are several active experimental techniques to directly measure the electron density but they require additional hardware. Alternatively, the electron density can be determined by measuring the Stark broadening of the spectral lines. The free electrons create an electric field, which broadens the lines via the Stark splitting of the degenerate energy levels [15]. The magnitude of the splitting is proportional to the strength of the electric field from the density of the electrons.

However, Stark broadening from free electrons is not the only source of line broadening; so the other sources must be understood such that the effect from the electron density can be isolated.

The other relevant sources of broadening for plasmas in this work are discussed here.

i) Spectral lines experience natural broadening as a result of the uncertainty in the time they will remain in an excited state, which due to the Heisenberg time-energy uncertainty principle [15]. This broadening is fit using a Lorentzian profile, and typically is larger for transitions with a high spontaneous emission coefficient.

ii) Doppler broadening is caused by the red or blue shift in wavelength because

of the Doppler effect of the thermal motion of the particles moving either toward or away from the spectrometer. This effect can be described by a Gaussian profile and is dominant at higher temperatures due to the increased thermal energy producing higher relative speeds [28].

iii) Particle collisions that disturb the electric field of an emitting particle decreases the uncertainty in the lifetime of the transition. As a result, the uncertainty of the energy in the transition increases which causes broadening. This is called pressure broadening and is proportional to the pressure of the plasma.

iv) As will be seen, the pressures involved in this work will render the pressure broadening term insignificant.

The Doppler broadening term will be small but not insignificant. In most cases, the Stark broadening term will be dominant but the Doppler term cannot be neglected so the broadening of the line will have contributions from multiple sources.

The Doppler broadening component can be fit using a Gaussian distribution and the Stark broadening component can be fit using a Lorentzian distribution. This is useful because a Voigt function is the combination of a Lorentzian curve, L(x), and a Gaussian curve, G(x). By fitting the observed emission line with a Voigt profile the individual components can be extracted to determine the contribution ratio from Stark broadening vs Doppler Broadening [15].

In principle, any line can be chosen to measure the broadening, however to relate the FWHM of the Stark broadening to the electron density requires the material specific impact parameter [28]. This work focuses on measuring the broadening of the Hydrogen-alpha (Hα) line. While hydrogen is not present in the target sample material there is a source from the atmospheric moisture.

The FWHM of the Hα line was related to the electron density using an experimentally derived fit produced by Surmick and Parigger [29]. The relationship is shown

below in Equation 9:

$$\Delta W_{\mathrm{H}\alpha}[nm] = 1.31(\frac{N_{\mathrm{e}}}{10^{17}})^{0.64\pm\ 0.03},$$

(9)

where ΔW is the FWHM, and N_{e} is the electron density.

By calculating and understanding the temperature and electron density of the plasma the results presented here can be related to other work and broader conclusions can be drawn.

III. Methodology

The experimental setup can be divided into four main components, the laser, the target, the spectrometer, and the schlieren. A diagram of the complete experimental setup is shown in Figure 24.

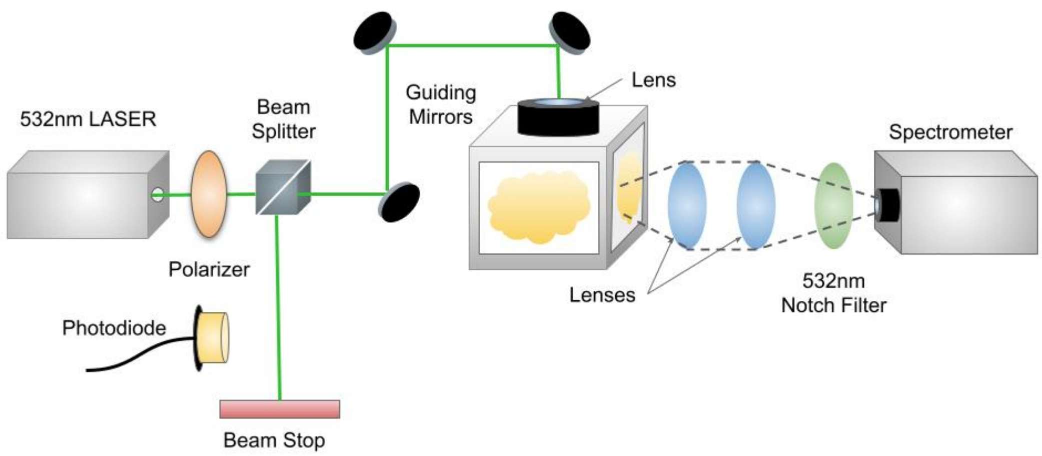

Figure 1. Schematic diagram of the experimental setup. The 532nm laser enters the vacuum cube from an access window on the top face.

The setup of each component is detailed below.

3.1 Ablation Targets

The ablation targets consisted of Cerium oxide (CeO_2) and Cerium hexaboride (CeB_6) discs purchased from Stanford Advanced Materials [30]. The CeO_2 had a purity of 99.99% with the principle impurity being La_2O_3 and other lanthanide oxides. The CeB_6 was 99.5% pure with the principle impurities being 261ppm Fe and 92ppm

identical mirror to the first to satisfy space requirements.

The beam was then uncollimated and focused by a 300mm focal length achromatic lens onto a razor blade knife-edge oriented horizontally. A 532nm notch filter was used to reduce the light from the laser flash and prevent it saturating the early images.

The images were captured using a Vision Research v12.1 High-Speed Camera operating at a resolution of 512x256 with the 512 pixels oriented horizontally. This was done to attempt to capture the shock waves from the laser pulse. Exposures were taken for $1\mu s$ at a rate of 40kHz which translates to one frame every $25\mu s$.

The LED intensity was varied until the gradients were well defined without significant saturation.

Spatial calibration was accomplished by placing a objects of known size in the frame. One image of the calibration target is shown in Figure 25.

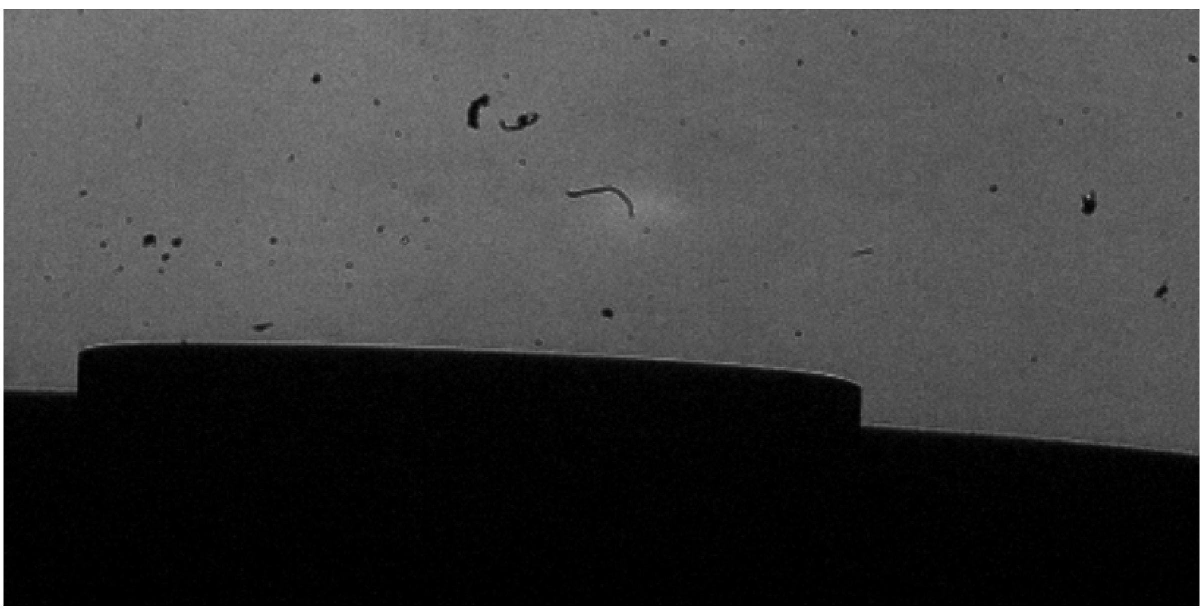

Figure 25. Schlieren image of a 1mm tall 20mm diameter round disc copper target. Artifacts were corrected in post-processing.

This gives a field of view of 15.1mm by 30.1mm.

1.2 Results

Schlieren images were recorded using the Phantom Camera Control software application [44] and were processed using ImageJ [45] with the cine viewer plugin [46].

The schlieren images contained artifacts from dust, debris and other defects on the optical components. These artifacts are present in all frames because they are not caused by transitory gradients, but instead by constant factors and thus they can be corrected for. The schlieren images were collected before the first pulse and this was used to create a flat frame subtraction to correct for the imperfections. A dark was taken to correct for the instrument effects and reduce noise [47].

An example of improvements from this correction is show in Figure 26.

Figure 26. Image of the calibration target before correction (top) and after flat, dark, and bias corrections (bottom). Corrections were only applied to rows above the pellet surface to preserve the surface location for reference.

Images were combined with the pixels intensities being averaged across the test shots.

The results from the schlieren imaging were primarily used in diagnostics and for qualitative assessment. This is because the frame rate, 40khz, translated to a frame period of $25\mu s$ per frame, this was too slow to permit much in the way of quantitative analysis. After testing, a majority of the experimental matrix was for times less than $5\mu s$. The first frame at $0\mu s$ shows only the laser pulse as a flash obscuring the frame. The second frame occurs at $25\mu s$ which is almost entirely obscured by the emission from the plasma. The third frame at $50\mu s$ is shown in Figure 27.

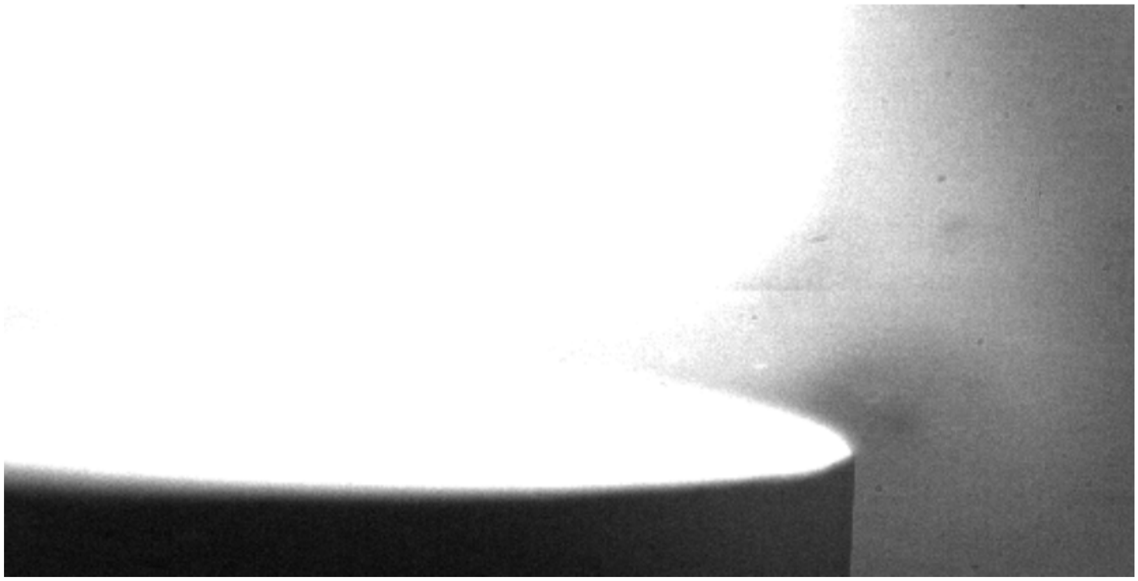

Figure 27. CeO_2 pellet 50μs after second laser pulse with artifact correction. A majority of the frame is obscured by the plasma emission.

The fourth frame at $75 \mu s$ is shown in Figure 28.

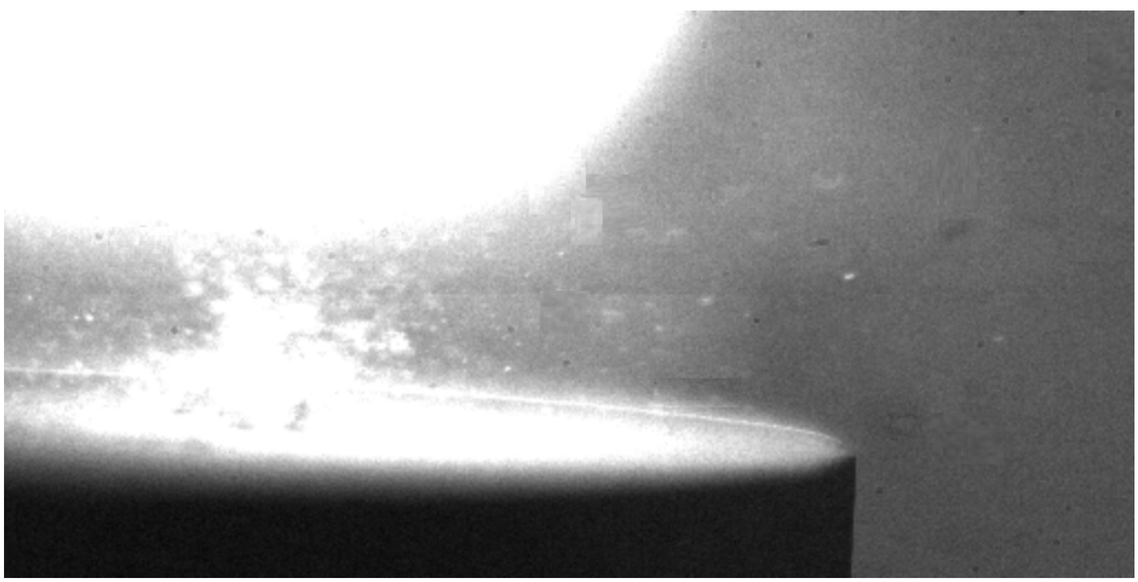

Figure 28. CeO_2 pellet 75μs after second laser pulse with artifact correction.

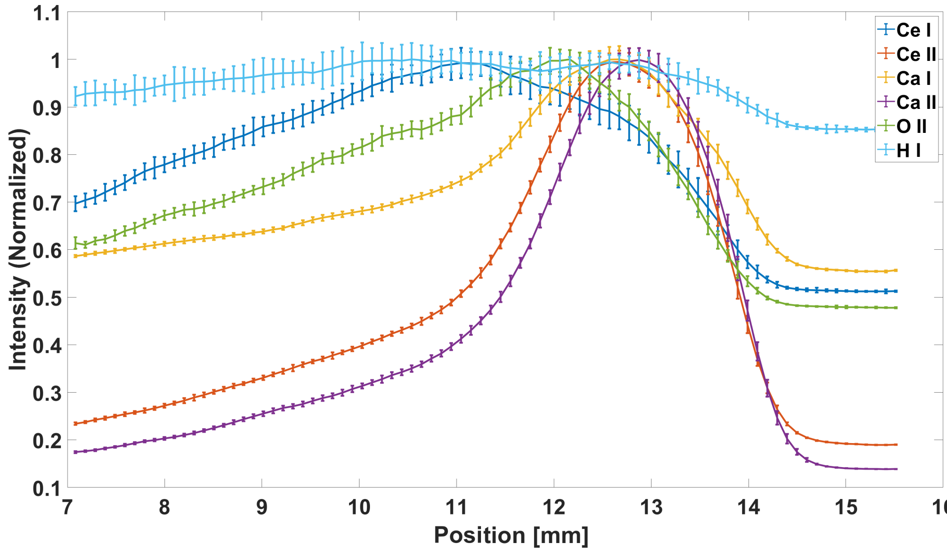

Figure 48. Plot of average normalized species' local distributions at 1750ns.

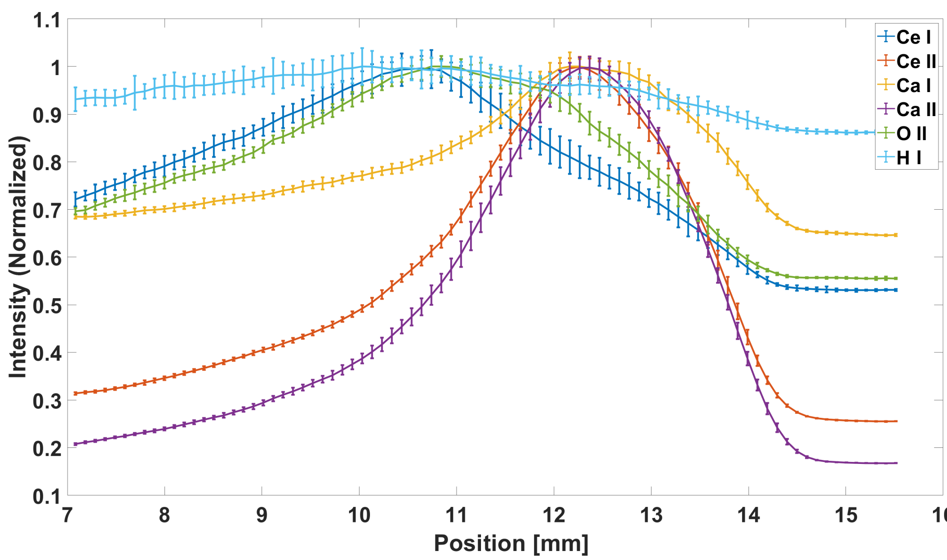

Figure 49. Plot of average normalized species' local distributions at 2000ns.

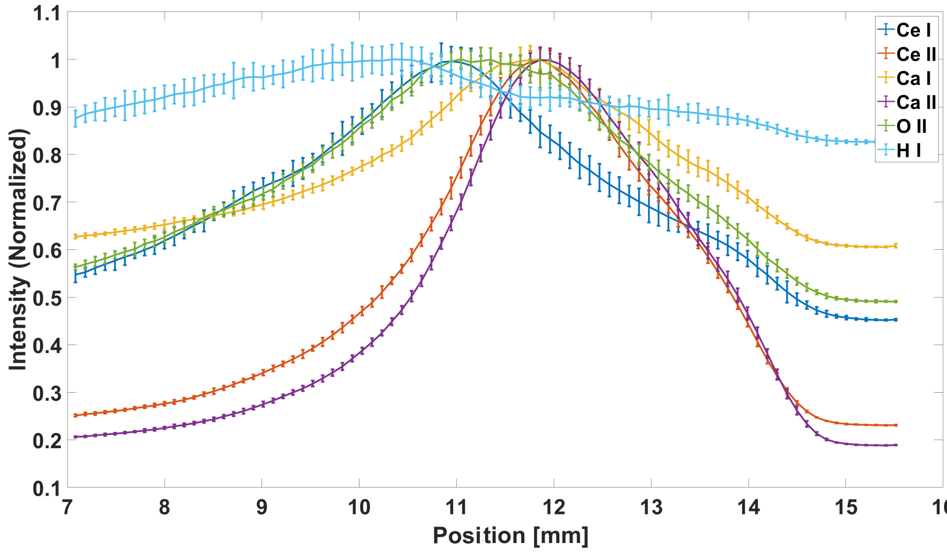

Figure 50. Plot of average normalized species' local distributions at 2500ns.

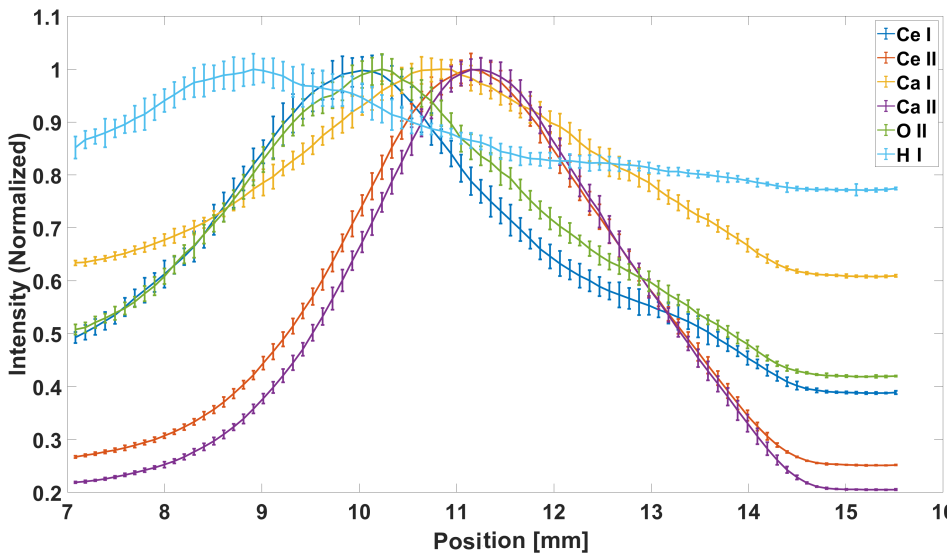

Figure 51. Plot of average normalized species' local distributions at 3000ns.

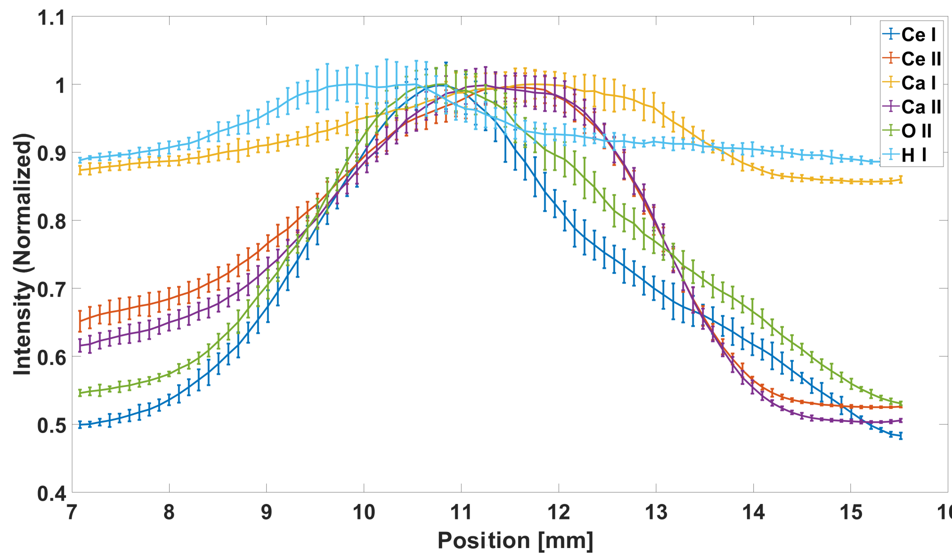

Figure 52. Plot of average normalized species' local distributions at 3500ns.

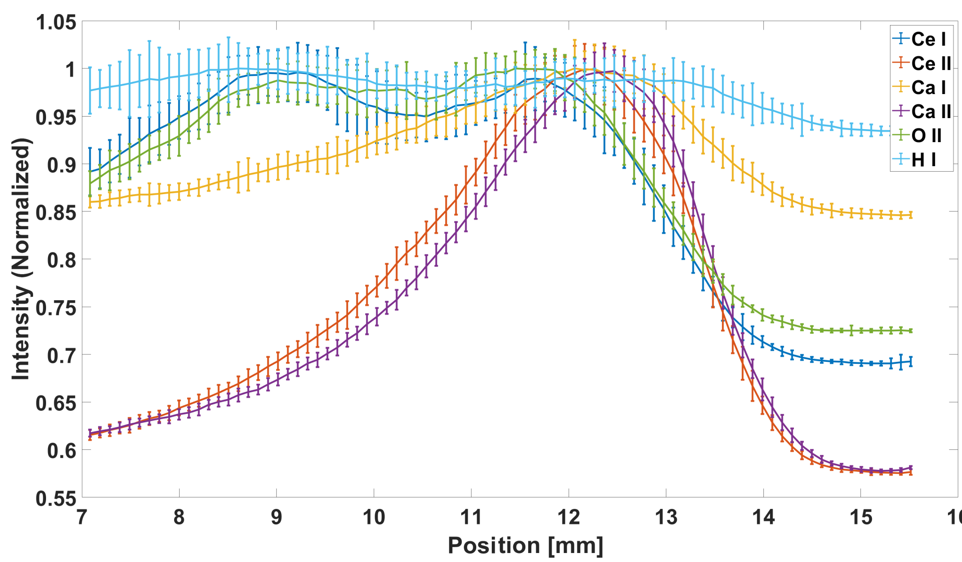

Figure 53. Plot of average normalized species' local distributions at 4000ns.

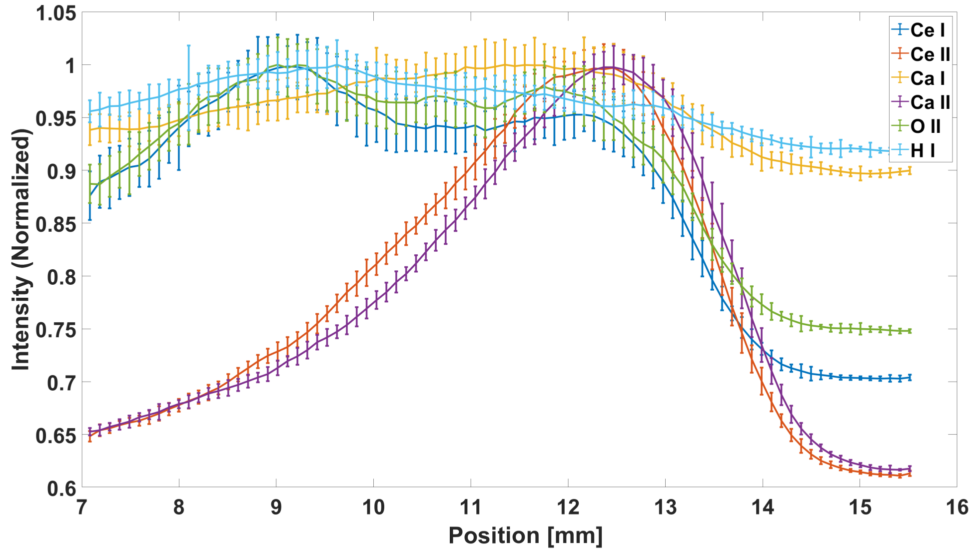

Figure 54. Plot of average normalized species' local distributions at 4500ns.

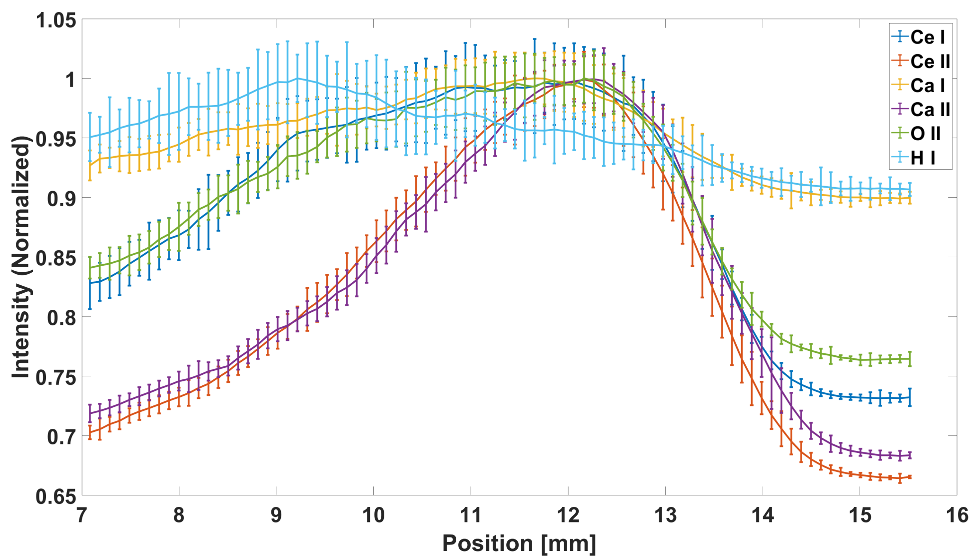

Figure 55. Plot of average normalized species' local distributions at 5000ns.

Bibliography

1. G. Ackerman, "Radiological/nuclear (rn) terrorism: Global assessment of threat intention drivers." 11 2016. [Online]. Available: https://www.osti.gov/biblio/1431197

2. M. J. Kristo and S. J. Tumey, "The state of nuclear forensics," *Nuclear Instruments and Methods in Physics Research Section B: Beam Interactions with Materials and Atoms*, vol. 294, pp. 656 – 661, 2013, proceedings of the Twelfth International Conference on Accelerator Mass Spectrometry, Wellington, New Zealand, 20-25 March 2011. [Online]. Available: http://www.sciencedirect.com/science/article/pii/S0168583X1200554X

3. C. J. Bridgman, *Introduction to the Physics of Nuclear Weapons Effects.* United States Air Force Institute of technology, 2001.

4. S. Glasstone, *The Effects of Nuclear Weapons.* United States Department of Energy, 1964.

5. E. W. Bierly and A. W. Klement, "Radioactive fallout from nuclear weapons tests," *Science*, vol. 147, no. 3661, p. 1057–1060, 1965.

6. C. Wallace, J. Bellucci, A. Simonetti, T. Hainley, E. Koeman, and P. Burns, "A multi-method approach for determination of radionuclide distribution in trinitite," *Journal of Radioanalytical and Nuclear Chemistry*, vol. 298, 11 2013.

7. A. J. Fahey, C. J. Zeissler, D. E. Newbury, J. Davis, and R. M. Lindstrom, "Postdetonation nuclear debris for attribution," *Proceedings of the National Academy of Sciences*, vol. 107, no. 47, pp. 20 207–20 212, 2010. [Online]. Available: https://www.pnas.org/content/107/47/20207

8. C. E. Bonamici, R. L. Hervig, and W. S. Kinman, "Tracking radionuclide fractionation in the first atomic explosion using stable elements," *Analytical Chemistry*, vol. 89, no. 18, pp. 9877–9883, 2017, pMID: 28810732. [Online]. Available: https://doi.org/10.1021/acs.analchem.7b01965

9. D. C. Christensen, "Pyrochemical recovery of plutonium from calcium fluoride reduction slag."

10. K. S. Holliday, J. M. Dierken, M. L. Monroe, M. A. Fitzgerald, N. E. Marks, R. C. Gostic, K. B. Knight, K. R. Czerwinski, I. D. Hutcheon, and J. W. McClory, "Plutonium segregation in glassy aerodynamic fallout from a nuclear weapon test," *Dalton Trans.*, vol. 46, pp. 1770–1778, 2017. [Online]. Available: http://dx.doi.org/10.1039/C6DT04184A

11. J. C. Marra, A. D. Cozzi, R. A. Pierce, J. M. Pareizs, A. R. Jurgensen, and D. M. Missimer, *Cerium as a Surrogate in the Plutonium Immobilized Form*. John Wiley Sons, Ltd, 2006, ch. 36, pp. 381–388. [Online]. Available: https://ceramics.onlinelibrary.wiley.com/doi/abs/10.1002/9781118371435.ch36

12. "Apparatus fundamentals," *Handbook of Laser-Induced Breakdown Spectroscopy*, p. 53–97, 2006.

13. D. N. Stratis, K. L. Eland, and S. M. Angel, "Dual-pulse LIBS: why are two lasers better than one?" in *Environmental Monitoring and Remediation Technologies II*, T. Vo-Dinh and R. L. Spellicy, Eds., vol. 3853, International Society for Optics and Photonics. SPIE, 1999, pp. 385 – 392. [Online]. Available: https://doi.org/10.1117/12.372877

14. W. Lochte-Holtgreven and H. Malamud, "Plasma diagnostics," *Physics Today*, vol. 23, no. 7, p. 72–72, 1970.

15. H.-J. Kunze, *Introduction to Plasma Spectroscopy.* Springer, Berlin, Heidelberg, 2001.

16. T. Fujimoto, "Plasma spectroscopy," *Plasma Polarization Spectroscopy Atomic, Optical, and Plasma Physics*, p. 29–49.

17. S. L. R. H. Huddlestone, *Plasma Diagnostic Techniques*, 1965.

18. G. Cristoforetti, A. De Giacomo, M. Dell'Aglio, S. Legnaioli, E. Tognoni, V. Palleschi, and N. Omenetto, "Local thermodynamic equilibrium in laser-induced breakdown spectroscopy: Beyond the mcwhirter criterion," *Spectrochimica Acta Part B: Atomic Spectroscopy*, vol. 65, no. 1, pp. 86 – 95, 2010. [Online]. Available: http://www.sciencedirect.com/science/article/pii/S0584854709003541

19. A. D. Giacomo, "Experimental characterization of metallic titanium-laser induced plasma by time and space resolved optical emission spectroscopy," *Spectrochimica Acta Part B: Atomic Spectroscopy*, vol. 58, no. 1, p. 71–83, 2003.

20. N. Sabri, Z. Haider, K. Tufail, F. D. Ismail, and J. Ali, "Spectroscopic diagnostics of laser induced plasma and self-absorption effects in al lines," *Physics of Plasmas*, vol. 25, p. 073303, 07 2018.

21. S. Zhang, X. Wang, M. He, Y. Jiang, B. Zhang, W. Hang, and B. Huang, "Laser-induced plasma temperature," *Spectrochimica Acta Part B: Atomic Spectroscopy*, vol. 97, pp. 13 – 33, 2014. [Online]. Available: http://www.sciencedirect.com/science/article/pii/S0584854714000615

22. C. H. C. W. F. Meggers and B. F. Scribner, *Tables of Spectral-Line Intensities, Part I – Arranged by Elements, Part II – Arranged by Wavelengths, Natl. Bur. Stand. Monograph 145.* Nat. Bur. Stand., U.S., 1975, vol. 42.

23. ——, *Tables of Spectral-Line Intensities, Part I – Arranged by Elements, Part II – Arranged by Wavelengths, Natl. Bur. Stand. Monograph 145.* Nat. Bur. Stand., U.S., 1975, vol. 42.

24. I. Wenaeker, “The spectrum of singly ionized oxygen, o ii,” *Phys. Scr.*, vol. 42, pp. 667–684, 1990.

25. G. Risberg, “The spectrum of atomic calcium, ca i, and extensions to the analysis of ca ii,” *Ark. Fys*, vol. 37, p. 231, 1968.

26. B. Edlén and P. Risberg, “The spectrum of singly-ionized calcium, ca ii,” *Ark. Fys*, vol. 10, pp. 553–566, 1956.

27. M. N. Saha and A. Fowler, “On a physical theory of stellar spectra,” *Proceedings of the Royal Society of London. Series A, Containing Papers of a Mathematical and Physical Character*, vol. 99, no. 697, pp. 135–153, 1921. [Online]. Available: https://royalsocietypublishing.org/doi/abs/10.1098/rspa.1921.0029

28. H. R. Griem, *Spectral line broadening by plasmas*, 1974.

29. D. Surmick and C. Parigger, “Empirical formulae for electron density diagnostics from halpha and hbeta line profiles,” *International Review of Atomic and Molecular Physics*, vol. 5, p. 73, 12 2014.

30. “Performance achromatic doublets, ar coated: 400 - 700nm,” Stanford Advanced Materials, 23661 Birtcher Dr. Lake Forest, CA 92630 U.S.A. [Online]. Available: https://www.samaterials.com

31. “Pubchem compound summary for cid 6093208, calcium hydroxide,” 2020. [Online]. Available: https://pubchem.ncbi.nlm.nih.gov/compound/Calcium-hydroxide

32. J. S. . S. B. .-. d. AJ Jr Effenberger, "Effect of atmospheric conditions on libs spectra," *Sensors (Basel)*, vol. 10, 2010. [Online]. Available: https://www.ncbi.nlm.nih.gov/pmc/articles/PMC3292154/

33. M. Young, "Imaging optics," in *Encyclopedia of Physical Science and Technology (Third Edition)*, third edition ed., R. A. Meyers, Ed. New York: Academic Press, 2003, pp. 645 – 660. [Online]. Available: http://www.sciencedirect.com/science/article/pii/B0122274105003288

34. "Performance achromatic doublets, ar coated: 400 - 700 nm," Thor Labs. [Online]. Available: https://www.thorlabs.com/newgrouppage9.cfm?objectgroup_id=120

35. "version 6.10.1.1903," Trenton, NJ, 2019.

36. W. Jansen, "Read / write .spe-files," MATLAB Central File Exchange. [Online]. Available: https://www.mathworks.com/matlabcentral/fileexchange/39959-read-write-spe-files

37. MATLAB, "version 9.7.0.1247435 (r2019b) update 2," Natick, Massachusetts, 2019.

38. G. V. Kuptsov, V. A. Petrov, V. V. Petrov, A. V. Laptev, A. V. Kirpichnikov, and E. V. Pestryakov, "Study of the temperature effect on the laser amplification process," in *XIV International Conference on Pulsed Lasers and Laser Applications*, V. F. Tarasenko, A. V. Klimkin, and M. V. Trigub, Eds., vol. 11322, International Society for Optics and Photonics. SPIE, 2019, pp. 186 – 190. [Online]. Available: https://doi.org/10.1117/12.2550839

39. C. E. Moore, *Selected Tables of Atomic Spectra, Atomic Energy Levels and Multiplet Tables – O I.* Nat. Bur. Stand., U.S., 1976. [Online]. Available: https://nvlpubs.nist.gov/nistpubs/Legacy/NSRDS/nbsnsrds3sec7.pdf

40. "Smooth data using moving average filter," Mathworks. [Online]. Available: https://www.mathworks.com/help/curvefit/smooth.html

41. D. of Physics and Astronomy, "Measurement and uncertainty analysis guide," University of North Carolina. [Online]. Available: https://physics.unc.edu/wp-content/uploads/sites/218/2018/07/Measurement-and-Uncertainty-Techniques.pdf

42. B. Campanella, S. Legnaioli, S. Pagnotta, F. Poggialini, and V. Palleschi, "Shock waves in laser-induced plasmas," *Atoms*, vol. 7, p. 57, 06 2019.

43. M. Ruzi, "voigt line shape fit," MATLAB Central File Exchange. [Online]. Available: https://www.mathworks.com/matlabcentral/fileexchange/57603-voigt-line-shape-fit

44. "Phantom camera control software." [Online]. Available: https://www.phantomhighspeed.com/resourcesandsupport/phantomresources/pccsoftware

45. S. R. M.D. Abramoff, P.J. Magalhaes, "Image processing with imagej," Biophotonics International, volume 11, issue 7, pp. 36-42, 2004.

46. T. Jordan, "Cine file importer," 2012. [Online]. Available: https://imagej.nih.gov/ij/plugins/cine-reader/index.html

47. "Flatfield correction." [Online]. Available: https://imagej.net/BigStitcher_Flatfield_correction

REPORT DOCUMENTATION PAGE	Form Approved OMB No. 0704–0188

1. REPORT DATE *(DD–MM–YYYY)*	**2. REPORT TYPE**	**3. DATES COVERED** *(From — To)*
26–03–2021	Master's Thesis	Aug 2020 — Mar 2021

4. TITLE AND SUBTITLE Characterization of the Spatial Distribution and Evolution of Cerium and Calcium in Laser Produced Plasma	**5a. CONTRACT NUMBER** **5b. GRANT NUMBER** **5c. PROGRAM ELEMENT NUMBER**
6. AUTHOR(S) Rynders, Michael G., 1st. Lt, USAF	**5d. PROJECT NUMBER** 0104555 **5e. TASK NUMBER** **5f. WORK UNIT NUMBER**
7. PERFORMING ORGANIZATION NAME(S) AND ADDRESS(ES) Air Force Institute of Technology Graduate School of Engineering an Management (AFIT/ENP) 2950 Hobson Way WPAFB OH 45433-7765	**8. PERFORMING ORGANIZATION REPORT NUMBER** AFIT-ENP-MS-21-M-132
9. SPONSORING / MONITORING AGENCY NAME(S) AND ADDRESS(ES) Air Force Research Laboratory	**10. SPONSOR/MONITOR'S ACRONYM(S)** AFIT/ENP **11. SPONSOR/MONITOR'S REPORT NUMBER(S)**

12. DISTRIBUTION / AVAILABILITY STATEMENT

DISTRIBUTION STATEMENT A:
APPROVED FOR PUBLIC RELEASE; DISTRIBUTION UNLIMITED.

13. SUPPLEMENTARY NOTES

14. ABSTRACT

Understanding plasma plumes and the distribution of plasma species microseconds after their formation has a variety of applications in fields such as hypersonics, explosion and combustion dynamics, and nuclear fireball chemistry. In this work, Laser Induced Breakdown Spectroscopy (LIBS) using double pulses of 532 nm light were used to analyze samples of cerium in atmospheres of air, vacuum, and argon. Cerium was used in this experiment to serve as a plutonium surrogate. CeO2 powder was pressed with CaO at 90-10 ratio to produce calcium doped pellets for use as sputtering targets. Inclusion of calcium impurities allowed the identification of how calcium species locate relative to cerium species in the plume. In addition, schlieren imaging at 40 kHz was used to attempt to capture the shockwave and to relate the plume development to the spatial location of the chemical species from the spectra. Tests were primarily conducted at 10 torr and over a time period 0 ns to 5000 ns after the second laser pulse. 1D spatial information was captured along the vertical center of the plasma plume over an 8.43 mm field of view. Temperature was estimated to be on the order of 3500K. Electron density was found to be on the order of 3×1016 cm-3. The species spatial distributions were found to show fractionation of the species. Establishing that Ce-II, Ca-I, and Ca-II tend to collocate in a plasma plume with Ce-I being located separately until recombination. This study will aid the understanding of physio-chemical processes involved fireball evolution.

15. SUBJECT TERMS

Cerium, LIBS, LPP

16. SECURITY CLASSIFICATION OF:			**17. LIMITATION OF ABSTRACT**	**18. NUMBER OF PAGES**	**19a. NAME OF RESPONSIBLE PERSON**
a. REPORT	**b. ABSTRACT**	**c. THIS PAGE**			Dr. Anil Patnaik , AFIT/ENP
U	U	U	UU	078	**19b. TELEPHONE NUMBER** *(include area code)* (937)-255-6565 x4532; Anil.Patnaik@afit.edu

Standard Form 298 (Rev. 8–98)
Prescribed by ANSI Std. Z39.18